Federico Salvadores*
Romina I. Minen*
Joaquin Carballada
Orlando M. Alfano
Maria M. Ballari

Universidad Nacional del Litoral and CONICET (INTEC), Santa Fe, Argentina.

Kinetic Study of Acetaldehyde Degradation Applying Visible Light Photocatalysis

A commercially available TiO_2 type (Kronos vlp 7000), doped with carbon and having an extended spectrum of light absorption wavelength, is investigated for photocatalytic degradation of a representative air pollutant, namely acetaldehyde, under visible light. The modeling of the studied system was carried out including the proposal of kinetic expressions for the contaminant degradation and generation of main intermediates based on the reaction mechanism, the mass balances in the reactor, and the lamps' superficial emission model to evaluate the radiation distribution in the reaction space. The predicted and experimental outlet concentrations of acetaldehyde and formaldehyde as main intermediate were found to be in good agreement obtaining a root mean square error equal to 13 %.

Keywords: Acetaldehyde, Air purification, Kinetic study, Photocatalysis, Visible light

Received: August 27, 2015; *revised:* October 27, 2015; *accepted:* November 02, 2015

DOI: 10.1002/ceat.201500507

Supporting Information available online

1 Introduction

The indoor air quality has a significant influence on human health due to the fact that people spend most of their time in these environments. A wide range of inorganic and organic pollutants like nitrogen oxides (NO and NO_2), sulfur dioxide (SO_2), and volatile organic compounds (VOCs) are emitted continuously to the indoor atmosphere or transferred from the outside of the buildings causing drowsiness, headache, sore throat, and mental fatigue. Accordingly, it is of vital importance to remove these contaminants in order to improve the wellness of indoor habitants. Acetaldehyde is a toxic, irritant, and probable carcinogen VOC contaminant in indoor and outdoor environments. It is a result of combustion processes, such as vehicle exhaust, tobacco smoke, and wood burning. Its main sources in homes include building materials, like laminate, linoleum, varnished wood, cork/pine flooring, plastic water-based and matt emulsion paints, as well as wooden, particleboard, plywood, and chipboard furniture. It is also created by thermal degradation of polymers in the plastics processing industry [1].

An alternative method for air quality control is heterogeneous photocatalytic oxidation employing titanium dioxide (TiO_2) as catalyst. However, normal TiO_2 can only be activated by UV radiation (200–400 nm) which represents approximately 4 % of the total sun energy whereas the visible light constitutes 45 % of the solar radiation. On the other hand, UV radiation is scarce in indoor lighting. To extend the use of photocatalytic oxidation to the visible light region, it is necessary to prolong the TiO_2 radiation absorption range to wavelengths corresponding to the visible spectrum (400–700 nm). So far, several methods of modifying TiO_2 photocatalysts to extend the absorption spectrum to visible radiation wavelengths have been investigated and, therefore, the applicability of the heterogeneous photocatalysis has been expanded [2, 3]. Moreover, several commercial types of modified TiO_2 can already be found in the market for indoor visible light applications.

Acetaldehyde degradation with conventional photocatalysis and UV radiation was studied in several works; in some of them the corresponding kinetic mechanism was proposed [4–9]. On the other hand, photocatalytic degradation of acetaldehyde was investigated employing modified TiO_2 for its application with visible light absorption [10–15].

There are many contributions on the photocatalytic degradation kinetics of various pollutants in the gas phase. However, most of them employ semi-empirical kinetic expressions in which model parameters depend on experimental conditions like the radiation flux, optical properties of the photocatalyst, pollutant concentration, relative humidity, reactor configuration etc. [6–9, 14]. Therefore, these kinetic equations are not applicable to other reactor configurations or under different operating conditions.

Here, a commercially available visible light absorption TiO_2 type doped with carbon (Kronos vlp 7000) was studied under visible light for photocatalytic degradation of acetaldehyde as a simple-structured organic contaminant of indoor air environments. The photocatalytic reaction was experimentally analyzed varying the main parameters of the system, such as the flow rate, relative humidity, pollutant concentration, and irradiance level. An intrinsic kinetic study on acetaldehyde oxidation and formation/degradation of the main intermediates was carried out. The kinetic expressions were derived from well-known mechanistic reaction steps, including the modeling of radiation absorption effects considering that photocatalytic reactions start with the activation of TiO_2 by photon absorption. The radiation model in the photoreactor includes: i) resolution of the lamps' radiation emission model, ii) determination of

Correspondence: Dr. Maria de los Milagros Ballari (ballari@santafe-conicet.gov.ar), Universidad Nacional del Litoral and CONICET (INTEC), Ruta Nacional No. 168, km 472.5, 3000 Santa Fe, Argentina.

*These authors contributed equally.

the immobilized catalyst optical properties, and iii) evaluation of the distribution of the local superficial rate of photon absorption (LSRPA). Finally, the kinetic parameters were estimated solving the mass balances of contaminant and main intermediates, including the radiation model in the photoreactor and employing the obtained experimental data. This kinetic model will be useful to predict the performance of large-scale gas-phase photocatalytic reactors employing the aforementioned commercial catalyst and visible radiation wavelengths.

2 Experimental

A visible light absorption photocatalyst doped with carbon (Kronos vlp 7000) was employed to perform the acetaldehyde degradation. The TiO_2 powder has over 87.5 % of anatase structure with a particle size of 15 nm, a specific surface area (BET) of 251 m^2g^{-1}, and 0.4–0.8 wt % elemental carbon at the surface [16]. More characteristics and properties of the commercial catalyst can be found in [16]. The immobilization of the TiO_2 powder was carried out according to a dip-coating procedure on a sand-blasted borosilicate glass plate. The TiO_2 powder concentration in deionized water for preparation of the coating was 75 g L^{-1}, and the pH, adjusted with nitric acid, was equal to 1. For every dip-coating cycle, the glass piece was dried at 110 °C for 24 h and calcined at 500 °C for 2 h, repeating this procedure four times.

The optical properties of the immobilized TiO_2 on the glass plate were determined as a function of wavelength between 300 and 600 nm in an Optronic OL Series 750 spectroradiometer equipped with an OL 740-70 integrating sphere reflectance attachment coated with polytetrafluoroethylene (PTFE). To evaluate the fraction of energy absorbed by the TiO_2 film, the spectral diffuse reflectance and the spectral diffuse transmittance of the coated glass were experimentally determined [17].

For degradation of the selected organic pollutant, namely acetaldehyde, a continuous planar photoreactor irradiated on both sides was employed. The coated glass plate was placed in the middle of the planar photoreactor, leaving two spaces on each side for gas circulation. The photocatalytic reactor was fed by certified PRAXAIR acetaldehyde gas stabilized in nitrogen (300 ppm) mixed with air to reach the desired inlet concentration, and irradiated with fluorescence visible-light lamps (Fig. 1). The irradiance flux on the reactor wall was measured with an ILT 1700 radiometer with a SED033/F/W visible-light sensor (400–1064 nm) and with a SED005/WBD320/W UVA sensor (300–400 nm).

The outlet and inlet contaminant concentrations of the reactor were analyzed employing a gas chromatograph with a flame ionization detector (FID) performing a direct injection of the gas sample. Tab. 1 summarizes the main characteristics, dimensions, and operating conditions of the employed experimental setup to carry out the acetaldehyde photocatalytic degradation experiments.

3 Theoretical Models

3.1 Kinetic Model

According to Sauer and Ollis [8], the global reaction pathway of the photocatalytic acetaldehyde degradation can be assumed as follows:

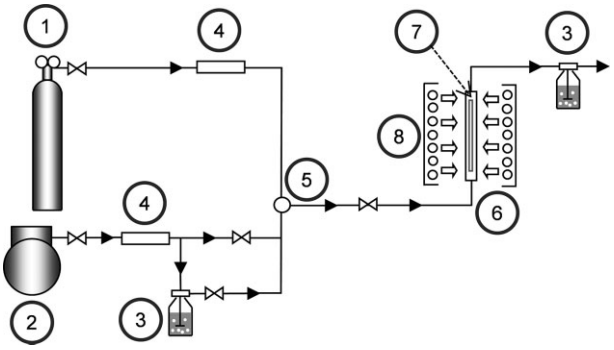

Figure 1. Experimental setup. (1) Acetaldehyde stabilized in N_2 (30 ppm); (2) compressor; (3) gas-washing bottle; (4) mass controllers; (5) temperature and relative humidity (RH) sensor; (6) reactor cell; (7) photocatalytic coated glass; (8) visible light source.

$$\text{Acetaldehyde} \rightarrow \text{Formaldehyde} \rightarrow \text{Formic Acid} \rightarrow CO_2 \quad (1)$$

However, in the studied system, only trace amounts of formaldehyde were detected and no formic acid was present within the detection limit of 8.3×10^{-9} mol L^{-1} for the developed analytical method. This indicates a good performance of the carbon-doped photocatalyst under visible light, showing a significant degradation of the pollutant. Carbon doping introduces new states close to the valence band edge of TiO_2 narrowing the photocatalyst band gap. In addition, a carbonaceous species at the surface of the photocatalyst facilitates the absorption in the visible wavelengths, and the high surface area of the doped TiO_2 promotes the adsorption of pollutants [3].

The extended degradation mechanism of acetaldehyde is presented in Tab. 2, together with the reaction rate expression for every reaction step. This reaction mechanism was adapted from Fujishima et al. [5] and Liang et al. [18] for acetaldehyde (CH_3CHO) degradation through the hydroxyl attack and the formation of several unstable radicals and finally formaldehyde (HCHO) (steps 4 to 7 in Tab. 2). The formaldehyde hydroxyl attack mechanism is extracted from Yang et al. [19] and the formic acid (HCOOH) degradation to carbon dioxide from Dijkstra et al. [20].

From this mechanism, the kinetic expressions for acetaldehyde and formaldehyde species can be derived according to the method provided in Supporting Information. The procedure considers the micro steady-state approximation for unstable or radical species and a Langmuir adsorption model with active site competition between water and stable gaseous species (see Tab. 2). In addition, the catalyst activation rate by radiation, i.e., first step in Tab. 2, can be assumed equal to the wavelength-averaged primary quantum yield ($\overline{\Phi}_\lambda$)[1)] multiplied by the LSRPA integrated over the useful wavelength range ($\int_\lambda e_s^a(x)\mathrm{d}\lambda$). The final expressions for the acetaldehyde and formaldehyde reaction rates are:

1) List of symbols at the end of the paper.

$$r_A = -\frac{\alpha_1\alpha_3 C_{W,gas} C_{A,gas}}{\left[2\alpha_3 C_{A,gas} + 2\alpha_4 C_{F,gas} + \alpha_2\left(1 + K_W C_{W,gas} + K_A C_{A,gas} + K_F C_{F,gas}\right)\right]\left(1 + K_W C_{W,gas} + K_A C_{A,gas} + K_F C_{F,gas}\right)} \times \left(\sqrt{1 + \frac{2\left(1 + K_W C_{W,gas} + K_A C_{A,gas} + K_F C_{F,gas}\right)}{\alpha_1 C_{W,gas}} \overline{\Phi}_\lambda \int_\lambda e_s^a(x)\mathrm{d}\lambda} - 1\right) \quad (2)$$

$$r_F = -\frac{\left(\alpha_3 C_{A,gas} - \alpha_4 C_{F,gas}\right)\alpha_1 C_{W,gas}}{\left[2\alpha_3 C_{A,gas} + 2\alpha_4 C_{F,gas} + \alpha_2\left(1 + K_W C_{W,gas} + K_A C_{A,gas} + K_F C_{F,gas}\right)\right]\left(1 + K_W C_{W,gas} + K_A C_{A,gas} + K_F C_{F,gas}\right)} \times \left(\sqrt{1 + \frac{2\left(1 + K_W C_{W,gas} + K_A C_{A,gas} + K_F C_{F,gas}\right)}{\alpha_1 C_{W,gas}} \overline{\Phi}_\lambda \int_\lambda e_s^a(x)\mathrm{d}\lambda} - 1\right) \quad (3)$$

Table 1. Photocatalyst properties, experimental setup characteristics, and operating conditions.

Reactor	Length	20 cm
	Width	10 cm
	Thickness	0.2 cm each side
	Volume	40 cm^3 each side
Photocat. sample	Photocatalyst	Kronos vlp 7000
	BET	251 $m^2 g^{-1}$
	Average particle size	15 nm
	Doped carbon amount	0.4–0.8 wt %
	Glass support length	20 cm
	Glass support width	10 cm
	Glass support thickness	0.3 cm
	TiO_2 specific deposited load	2.3×10^{-4} g cm^{-2}
	TiO_2 film thickness (estimated)	$3.4–4.4\times10^{-5}$ cm
Visible lamps		GE F4T5/CW×14
	Input power	4 W
	Emission wavelength	380–720 nm
Temperature		21–24 °C
Flow rate		1000–3000 $cm^3 min^{-1}$
Relative humidity		10–70 %
Irradiance flux	Visible	23–64 W m^{-2} each side
	UV	0.7–2 W m^{-2} each side
Inlet pollutant concentration		1.0×10^{-7} – 4.1×10^{-7} mol L^{-1}

where

$$\alpha_1 = \frac{k_1 k_2 K_W [O_2][S]}{2k_{12}} \quad (4)$$

$$\alpha_2 = \frac{k_{13}[M]}{[S]} \quad (5)$$

$$\alpha_3 = k_3 K_A \quad (6)$$

$$\alpha_4 = k_8 K_F \quad (7)$$

Eqs. (2) and (3) can be simplified considering that acetaldehyde and formaldehyde concentrations are much lower than the water concentration in the gas phase. Then, the following simplified kinetic expressions can be obtained:

$$r_A = -\frac{\beta_1 C_{A,gas} C_{W,gas}}{\left(1 + K_W C_{W,gas}\right)^2} \times \left(\sqrt{1 + \frac{2\left(1 + K_W C_{W,gas}\right)}{C_{W,gas}} \beta_2 \int_\lambda e_s^a(x)\mathrm{d}\lambda} - 1\right) \quad (8)$$

Table 2. Acetaldehyde photocatalytic degradation mechanism.

Step		Reaction	Reaction rate
0	Activation	$TiO_2 + h\nu \rightarrow e^- + h^+$	$r_g = \overline{\Phi}_\lambda \int_\lambda e^a_{s,\lambda}(\underline{x})\,d\lambda$
1	Hole trap	$h^+ + H_2O_{ads} \rightarrow HO^\bullet + H^+$	$r_1 = k_1[H_2O]_{ads}[h^+]$
2	Electron capture	$e^- + O_2 \rightarrow O_2^{\bullet-}$	$r_2 = k_2[O_2][e^-]$
3	Radical attack to acetaldehyde	$CH_3CHO_{ads} + HO^\bullet \rightarrow CH_3CO^\bullet + H_2O$	$r_3 = k_3[CH_3CHO]_{ads}[HO^\bullet]$
4		$CH_3CO^\bullet + {}^1/_2\,O_2 \rightarrow CH_3COO^\bullet$	$r_4 = k_4[CH_3CO^\bullet][O_2]^{1/2}$
5		$CH_3COO^\bullet \rightarrow CH_3^\bullet + CO_2$	$r_5 = k_5[CH_3COO^\bullet]$
6		$CH_3^\bullet + O_2 \rightarrow CH_3OO^\bullet$	$r_6 = k_6[CH_3^\bullet][O_2]$
7		$CH_3OO^\bullet + HO^\bullet \rightarrow HCHO_{ads} + H_2O + {}^1/_2\,O_2$	$r_7 = k_7[CH_3OO^\bullet][HO^\bullet]$
8	Radical attack to formaldehyde	$HCHO_{ads} + HO^\bullet \rightarrow HCO^\bullet + H_2O$	$r_8 = k_8[HCHO]_{ads}[HO^\bullet]$
9		$HCO^\bullet + HO^\bullet \rightarrow HCOOH_{ads}$	$r_9 = k_9[HCO^\bullet][HO^\bullet]$
10	Radical attack to formic acid	$HCOOH_{ads} + HO^\bullet \rightarrow HCOO^\bullet + H_2O$	$r_{10} = k_{10}[HCOOH]_{ads}[HO^\bullet]$
11		$HCOO^\bullet + O_2 \rightarrow CO_2 + H^+ + O_2^{\bullet-}$	$r_{11} = k_{11}[HCOO^\bullet][O_2]$
12	Recombination	$e^- + h^+ \rightarrow$ heat	$r_{12} = k_{12}[e^-][h^+]$
13	Radical termination	$HO^\bullet + M \rightarrow$ products	$r_{13} = k_{13}[M][HO^\bullet]$
14	Water adsorption	$H_2O_{gas} + \text{sites} \rightleftharpoons H_2O_{ads}$	$[H_2O]_{ads} = \frac{K_W[H_2O]_{gas}[S]}{1+K_W[H_2O]_{gas}+K_A[CH_3CHO]_{gas}+K_F[HCHO]_{gas}}$
15	Acetaldehyde adsorption	$CH_3CHO_{gas} + \text{sites} \rightleftharpoons CH_3CHO_{ads}$	$[CH_3CHO]_{ads} = \frac{K_A[CH_3CHO]_{gas}[S]}{1+K_W[H_2O]_{gas}+K_A[CH_3CHO]_{gas}+K_F[HCHO]_{gas}}$
16	Formaldehyde adsorption	$HCHO_{gas} + \text{sites} \rightleftharpoons HCHO_{ads}$	$[HCHO]_{ads} = \frac{K_F[HCHO]_{gas}[S]}{1+K_W[H_2O]_{gas}+K_A[CH_3CHO]_{gas}+K_F[HCHO]_{gas}}$

$$r_F = -\frac{(\beta_1 C_{A,gas} - \beta_3 C_{F,gas}) C_{W,gas}}{(1 + K_W C_{W,gas})^2} \times \left(\sqrt{1 + \frac{2(1 + K_W C_{W,gas})}{C_{W,gas}} \beta_2 \int_\lambda e^a_s(x)\,d\lambda} - 1 \right) \quad (9)$$

where

$$\beta_1 = \frac{\alpha_1 \alpha_3}{\alpha_2} \quad (10)$$

$$\beta_2 = \frac{\overline{\Phi}_\lambda}{\alpha_1} \quad (11)$$

$$\beta_3 = \frac{\alpha_1 \alpha_4}{\alpha_2} \quad (12)$$

3.2 Radiation Model

In order to evaluate the LSRPA (e_s^a) at each point on the catalytic wall, used in Eqs. (8) and (9), the lamps' emission model was solved.

The local net radiation flux on the catalytic film corresponding to a wavelength λ is defined by [21]:

$$q_\lambda(\underline{x}) = \underline{q}_\lambda(\underline{x}) \cdot \underline{n}_g = \int_0^{2\pi} I_\lambda(\underline{x}, \underline{\Omega})\, \underline{\Omega} \cdot \underline{n}_g\, d\Omega \quad (13)$$

where $\underline{n}_g$ is the outwardly directed unit vector normal to the catalytic film and I_λ is the radiation intensity associated to a beam of rays carrying energy of wavelength λ in the direction of the unit vector $\underline{\Omega}$ corresponding to the solid angle Ω.

According to the coordinate system adopted in Fig. 2 and considering the contribution of all lamps and all emitted wavelengths, the local net radiation flux on the catalytic film results as:

$$q_i(\underline{x}) = \sum_{\lambda=380}^{720} \sum_{i=1}^{7} \int_{\phi_{min}}^{\phi_{max}} \int_{\theta_{min}}^{\theta_{max}} I_{\lambda,L_i}(\underline{x}, \theta, \phi) \sin^2\phi \sin\theta\, d\theta\, d\phi \quad (14)$$

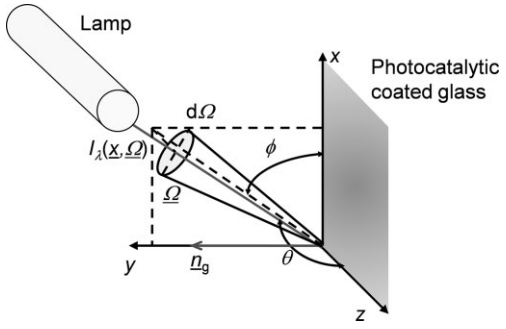

Figure 2. Adopted coordinate system.

Since the radiation intensity arriving from each lamp comes from the directions defined by the vision angle for each catalytic wall position, it follows:

$$I_\lambda(\underline{x},\theta,\phi) = \begin{cases} 0 & \theta,\phi < \theta_{\min},\phi_{\min} \\ I_{\lambda,\mathrm{L}_i}(\underline{x},\theta,\phi) & \theta_{\min},\phi_{\min} < \theta,\phi < \theta_{\max},\phi_{\max} \\ 0 & \theta,\phi > \theta_{\max},\phi_{\max} \end{cases} \tag{15}$$

The boundary condition for the lamp emission model is [22]:

$$I_{\lambda,\mathrm{L}_i}(\underline{x},\theta,\phi) = \frac{P_\lambda}{2\pi^2 r_\mathrm{L} z_\mathrm{L}} \tag{16}$$

where P_λ is the spectral emission power of each lamp, and r_L and z_L are the radius and length of the lamp, respectively. The values of the integration limits in Eq. (14) for the employed emission system are provided in the Supporting Information.

According to Fig. 3, the LSRPA on one immobilized catalyst film, e.g., on layer number 1, is given by the absorption of the direct and indirect radiation:

$$e^a_{\mathrm{s},\lambda,1}(\underline{x}) = A_{\mathrm{TiO_2},\lambda} q_{\mathrm{i},\lambda}(\underline{x}) + A_{\mathrm{TiO_2},\lambda} q^-_{1,\lambda}(\underline{x}) \tag{17}$$

where $A_{\mathrm{TiO_2},\lambda}$ is the absorption radiation fraction of the catalytic film.

Applying a radiative flux balance in each layer of Fig. 3 leads to:

$$q^-_{n-1,\lambda} = R_{n,\lambda} q^+_{n-1,\lambda} + T_{n,\lambda} q^-_{n,\lambda} \qquad n = 1,2,3 \tag{18}$$

where $T_{n,\lambda}$ and $R_{n,\lambda}$ are the diffuse transmittance and reflectance of the n-th layer, respectively. Then, the indirect radiation flux that reaches layer 1 can be obtained by the following expression:

$$q^-_{1,\lambda}(\underline{x}) = q_{\mathrm{i},\lambda}(\underline{x}) \frac{R_{\mathrm{g},\lambda} T_{\mathrm{TiO_2},\lambda} - R^2_{\mathrm{g},\lambda} R_{\mathrm{TiO_2},\lambda} T_{\mathrm{TiO_2},\lambda} + T_{\mathrm{g},\lambda} T_{\mathrm{TiO_2},\lambda} + T^2_{\mathrm{g},\lambda} R_{\mathrm{TiO_2},\lambda} T_{\mathrm{TiO_2},\lambda}}{1 - 2R_{\mathrm{g},\lambda} R_{\mathrm{TiO_2},\lambda} + R^2_{\mathrm{g},\lambda} R^2_{\mathrm{TiO_2},\lambda} - T^2_{\mathrm{g},\lambda} R^2_{\mathrm{TiO_2},\lambda}} \tag{19}$$

Replacing Eq. (19) in Eq. (17), the LSRPA is given by:

$$e^a_{\mathrm{s},\lambda,1}(\underline{x}) = A_{\mathrm{TiO_2},\lambda} q_{\mathrm{i},\lambda}(\underline{x}) \left[1 + \frac{R_{\mathrm{g},\lambda} T_{\mathrm{TiO_2},\lambda} - R^2_{\mathrm{g},\lambda} R_{\mathrm{TiO_2},\lambda} T_{\mathrm{TiO_2},\lambda} + T_{\mathrm{g},\lambda} T_{\mathrm{TiO_2},\lambda} + T^2_{\mathrm{g},\lambda} R_{\mathrm{TiO_2},\lambda} T_{\mathrm{TiO_2},\lambda}}{1 - 2R_{\mathrm{g},\lambda} R_{\mathrm{TiO_2},\lambda} + R^2_{\mathrm{g},\lambda} R^2_{\mathrm{TiO_2},\lambda} - T^2_{\mathrm{g},\lambda} R^2_{\mathrm{TiO_2},\lambda}} \right] \tag{20}$$

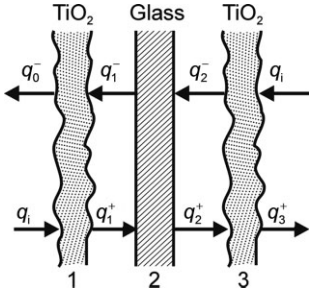

Figure 3. Schematic representation of the immobilized TiO_2 on glass and the radiation transfer through it.

The optical properties of the immobilized catalyst used in Eq. (20) were calculated according to the methodology developed by Edwards [23] and using experimental measurements of the diffuse transmittance and reflectance of the borosilicate glass and the coated glass on both sides with TiO_2 (T_g, $T_{\mathrm{TiO_2,g,TiO_2}}$, R_g, and $R_{\mathrm{TiO_2,g,TiO_2}}$ respectively):

$$R_{\mathrm{TiO_2}} = \frac{R_{\mathrm{TiO_2,g,TiO_2}} T_\mathrm{g} - T_{\mathrm{TiO_2,g,TiO_2}} R_\mathrm{g}}{T_{\mathrm{TiO_2,g,TiO_2}} T^2_\mathrm{g} - T_{\mathrm{TiO_2,g,TiO_2}} R^2_\mathrm{g} + T_\mathrm{g}} \tag{21}$$

$$T_{\mathrm{TiO_2}} = \sqrt{\frac{\left(R_{\mathrm{TiO_2,g,TiO_2}} - R_{\mathrm{TiO_2}}\right)\left[1 - R_{\mathrm{TiO_2}}\left(R_\mathrm{g} + \frac{T^2_\mathrm{g} R_{\mathrm{TiO_2}}}{1 - R_\mathrm{g} R_{\mathrm{TiO_2}}}\right)\right]}{R_\mathrm{g} + \frac{T^2_\mathrm{g} R_{\mathrm{TiO_2}}}{1 - R_\mathrm{g} R_{\mathrm{TiO_2}}}}} \tag{22}$$

Afterwards, the absorption radiation fraction can be calculated as follows [24]:

$$A_{\mathrm{TiO_2}} = 1 - R_{\mathrm{TiO_2}} - T_{\mathrm{TiO_2}} \tag{23}$$

3.3 Mass Balances

Considering that the flow reactor is not controlled by the interfacial mass transport, a 1D convection-controlled model can be assumed for the acetaldehyde and formaldehyde mass balance equations:

$$v_\mathrm{air} \frac{\mathrm{d}C_{\mathrm{A,gas}}}{\mathrm{d}x} = a_v \langle r_\mathrm{A} \rangle_\mathrm{W} \tag{24}$$

$$v_{air}\frac{dC_{F,gas}}{dx} = a_v\langle r_F\rangle_W \quad (25)$$

where a_v is the active surface area per unit reactor volume:

$$a_v = \frac{A_{act}}{V_R} \approx \frac{1}{e} \quad (26)$$

The corresponding inlet conditions are given by:

$$C_{A,gas}(x=0) = C_{A,in} \quad (27)$$

$$C_{F,gas}(x=0) = 0 \quad (28)$$

In order to pose the previous mass balances, it was verified that the reaction rate is much slower than the interfacial mass transfer [25]:

$$\frac{\langle r_A\rangle}{k_s\langle C_{A,gas}\rangle} \approx 3.3\times10^{-2} < 0.1 \quad (29)$$

The average reaction rate in the photoreactor volume was calculated as follows:

$$\langle r_A\rangle = \frac{Q\left(C_{A,in} - C_{A,out}\right)}{A_{act}} \quad (30)$$

where A_{act} can be considered as the catalytic plate area. Then, the maximum average acetaldehyde degradation rate reached in this work is around 4.4×10^{-10} mol cm^{-2}min^{-1}.

On the other hand, the external mass transfer coefficient was calculated from:

$$Sh = \frac{k_s\, L_c}{D_{A-air}} \quad (31)$$

Shah and London [26] proposed that for slits with one exchanging side the Sherwood number (Sh) can be taken as equal to 5. For a characteristic length (L_c) equal to the hydraulic diameter of the photoreactor and a diffusion coefficient of acetaldehyde in air ($D_{A\text{-}air}$) of 7.7 cm^{2}min^{-1}, the calculated external mass transfer coefficient (k_s) was 97.9 cm min^{-1}.

4 Results and Discussion

The measurements of the spectral diffuse reflectance and transmittance of the coated glass with TiO_2 are presented in Fig. 4 a. The calculated absorption fraction for the tested sample compared with the spectral emission distribution of the employed lamps can be found in Fig. 4 b.

The double integral of Eq. (14) for the calculation of the local net radiation flux on the catalytic wall was solved numerically and compared with the experimental values. These results are shown in Fig. 5, obtaining a total root mean square error (RMSE) between experimental data and model predictions of 10.86 %.

The calculated LSRPA according to Eq. (20) was averaged over the width of the reactor obtaining the axial profile of the absorbed radiation, indicated in Fig. 6. This W-averaged LSRPA along the reactor was applied in the 1D mass balance model of Eqs. (24) and (25).

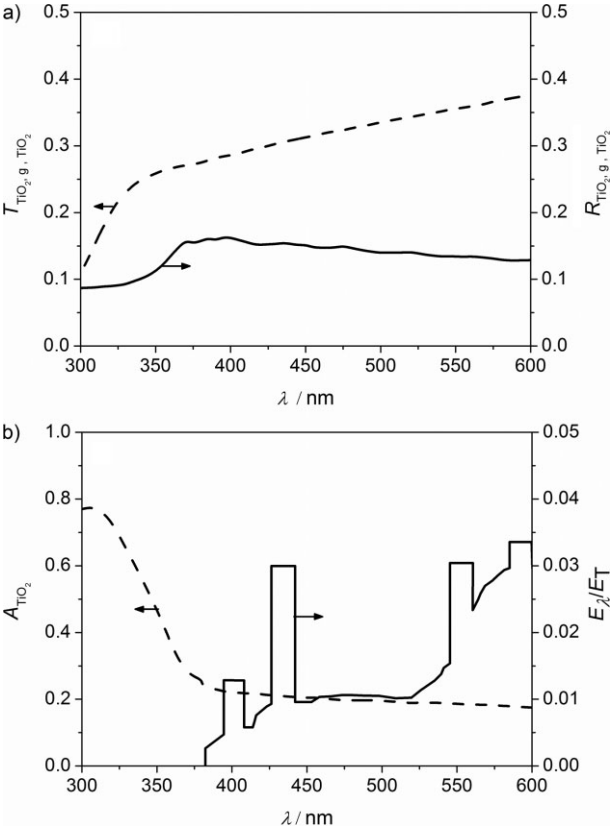

Figure 4. (a) Experimental spectral diffuse transmittance and reflectance of the coated glass on both sides with TiO_2. (b) Calculated spectral fraction of energy absorbed by the immobilized TiO_2 film and the spectral emission distribution of the employed visible lamps.

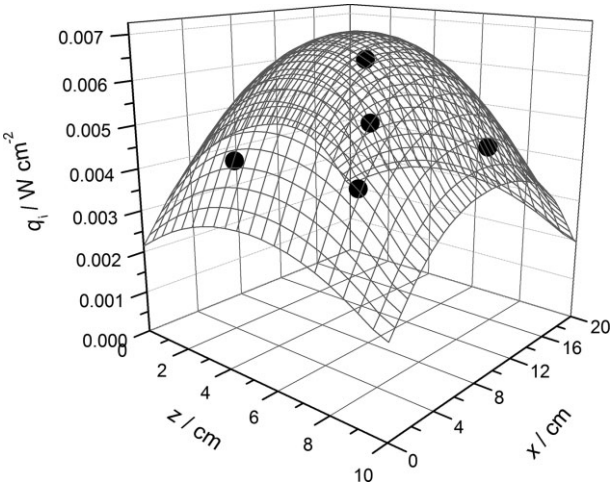

Figure 5. Experimental and predicted incident radiation flux on the immobilized TiO_2 sample.

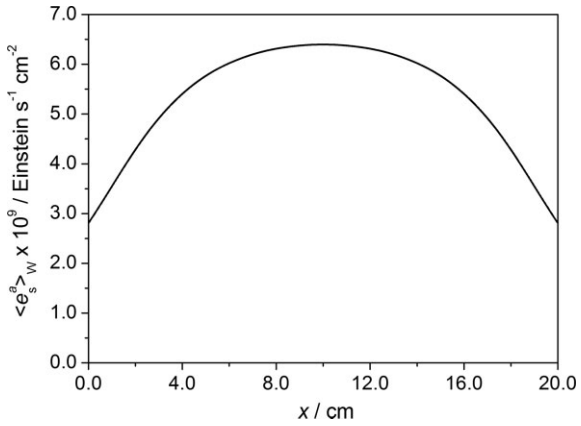

Figure 6. W-averaged LSRPA along the reactor.

Solving numerically the acetaldehyde and formaldehyde coupled mass balances and comparing the results with the experimental data under different operating conditions, the kinetic parameters were estimated by means of a nonlinear optimization tool. The estimated kinetic parameters are listed in Tab. 3.

Table 3. Estimated kinetic parameters.

Parameter	Value	Units
β_1	1.116×10^{4}	$cm^4min^{-1}mol^{-1}$
β_2	7.193×10^{-4}	$mol\,s\,cm^{-1}E^{-1}$
β_3	1.035×10^{5}	$cm^4min^{-1}mol^{-1}$
K_w	2.594	cm^3mol^{-1}

The simulation results obtained with the estimated kinetic parameters and the experimental acetaldehyde and formaldehyde outlet concentrations at the reactor steady state, as well as their associated error, are compared in Figs. 7 to 10. The total RMSE between the experimental and simulated data was 13.63 %, indicating a good agreement between computed and experimental values.

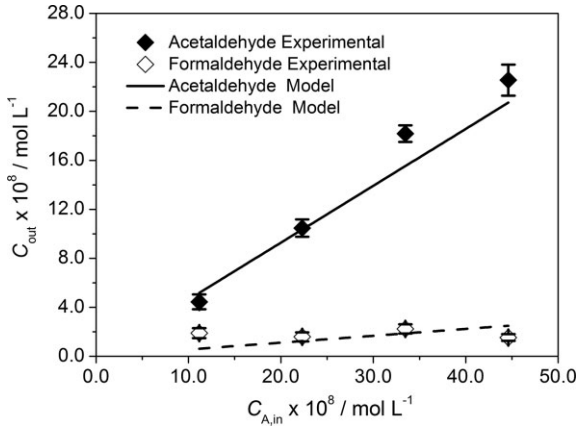

Figure 7. Simulated and experimental outlet concentrations of acetaldehyde and formaldehyde varying the inlet acetaldehyde concentration.

As mentioned before, different operating conditions of the system were varied in order to observe their effect on the photocatalytic reaction rate. The employed pivot conditions for the different experiments were: $C_{A,in} = 2.1\times10^{-7}\,mol\,L^{-1}$, $RH = 50\,\%$, $q_i = 64\,W\,m^{-2}$ on each side of the reactor, and $Q = 1\,L\,min^{-1}$.

When the inlet concentration of the pollutant increases, the acetaldehyde outlet concentration rises as well (Fig. 7). However, modifying the initial concentration of the pollutant, the final conversion of the reacting system does not change, indicating an almost first-order kinetics with the pollutant concentration.

In Fig. 8, when the relative humidity is increased, water vapor competes with acetaldehyde for the same active sites and the pollutant consumption declines.

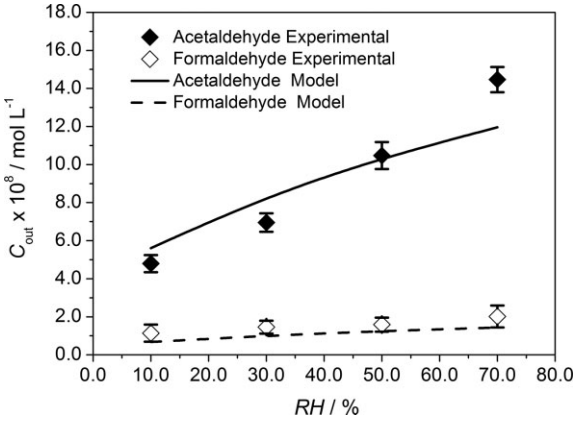

Figure 8. Simulated and experimental outlet concentrations of acetaldehyde and formaldehyde varying the relative humidity.

The effect of radiation power on the acetaldehyde and formaldehyde outlet concentrations is illustrated in Fig. 9. When the irradiance is decreased to 50 % and 35 % by placing neutral filters between the lamps and the photocatalytic plate, a lower conversion of the pollutant is observed because less electrons and holes are produced during the photocatalyst activation stage and, therefore, less hydroxyl radicals are formed.

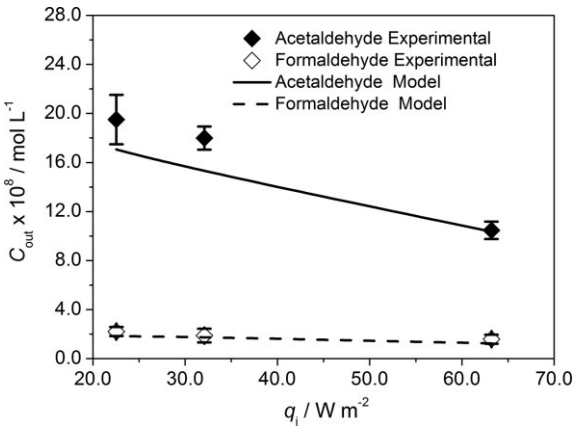

Figure 9. Simulated and experimental outlet concentrations of acetaldehyde and formaldehyde varying the incident radiation flux.

Finally, Fig. 10 demonstrates that when the flow rate is increased, the residence time in the reactor decreases. Therefore, for low flow rates a larger conversion of the pollutant is observed.

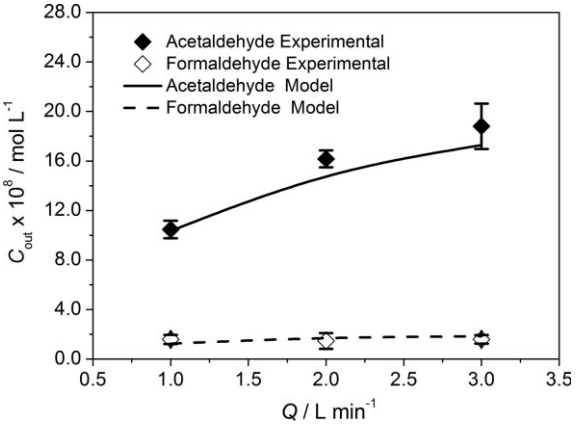

Figure 10. Simulated and experimental outlet concentrations of acetaldehyde and formaldehyde varying the flow rate.

In the experiments conducted under different operating conditions, several pollutant conversions were achieved with a minimum near 3 % for the lowest irradiation condition and a maximum around 73 % employing the highest incident radiation flux and lowest relative humidity.

5 Conclusions

A kinetic study based on the reaction mechanism of acetaldehyde degradation in the gas phase applying visible light was carried out. The predictions of the proposed model for the outlet acetaldehyde concentration employing the estimated kinetic parameters are in good agreement with the experimental values, with an RMSE of 13.63 %. Applying a lamp superficial emission model, the absorbed radiation rate on the photocatalytic reactor wall was evaluated and included in the photocatalytic kinetic model. A good correlation between the experimental data and predicted values of the incident radiation flux was obtained, with an RMSE of 10.86 %.

Under the different operating conditions employed in this work, a significant acetaldehyde conversion, i.e., 73 %, was observed with a small amount of formaldehyde formation as the main stable intermediate of the photocatalytic reaction. The good photocatalytic performance of carbon-doped TiO_2 under visible light provides promising results for a real-scale air treatment under indoor conditions.

Acknowledgment

Financial support from the Universidad Nacional del Litoral, CONICET, and Agencia Nacional de Promoción Científica y Tecnológica is gratefully acknowledged. Antonio Negro, Juan Andini, Claudio Passalía, and Eduardo Vidal are acknowledged for their help in experimental work. Kronos is thanked for the provided photocatalyst.

The authors have declared no conflict of interest.

Symbols used

A	[–]	fraction of energy absorbed
A_{act}	[cm^2]	catalytic active area
a_v	[cm^{-1}]	active area per unit reactor volume
C	[mol L^{-1}]	concentration
D	[$cm^2 min^{-1}$]	diffusion coefficient
e	[cm]	reactor thickness
e^-	[–]	electron
e_s^a	[E $s^{-1} cm^{-2}$]	local superficial rate of photon absorption
E	[J]	radiant energy
h^+	[–]	hole
I	[E $s^{-1} cm^{-2} sr^{-1}$]	specific radiation intensity
k	[–]	reaction rate constant, units depend on the reaction step
k_s	[cm min^{-1}]	external mass transfer coefficient
K	[$cm^3 mol^{-1}$]	adsorption equilibrium constant
L_c	[cm]	characteristic length
M	[–]	inert material involved in termination reactions
$\underline{n}_g$	[–]	outwardly directed unit normal vector to the catalytic film
P	[W]	lamp emission power
q	[W cm^{-2}]	local net radiation flux
$\underline{q}$	[W cm^{-2}]	local radiation flux vector
Q	[L min^{-1}]	flow rate
r	[mol $cm^{-2} min^{-1}$]	superficial reaction rate
r_L	[cm]	lamp radius
R	[–]	reflectance
RH	[%]	relative humidity
S	[–]	catalytic active site
Sh	[–]	Sherwood number
T	[–]	transmittance
v	[cm min^{-1}]	velocity
V	[L]	reactor volume
x	[cm]	Cartesian coordinate
$\underline{x}$	[cm]	position vector
y	[cm]	Cartesian coordinate
z	[cm]	Cartesian coordinate
z_L	[cm]	lamp length

Greek letters

α, β	[–]	kinetic parameters, units depend on the group of constants
ϕ	[rad]	spherical coordinate
Φ	[mol E^{-1}]	quantum yield
λ	[nm]	wavelength

θ	[rad]	spherical coordinate
Ω	[sr]	solid angle
$\underline{\Omega}$	[–]	unit vector in the direction of radiation propagation

Subscripts

A	acetaldehyde
act	active
ads	adsorption
air	air
F	formaldehyde
g	glass or generation
gas	gas phase
i	relative to the incident radiation flux
in	inlet condition
L	relative to the lamps
max	maximum limit value
min	minimum limit value
out	outlet condition
R	reactor
s	relative to the catalytic surface or wall
T	total
W	water or relative to the reactor width
λ	wavelength

Special symbols

[ ]	[mol cm^{-3} or mol cm^{-2}]	volumetric or superficial concentration of specific species
$\langle\rangle$		average value over a defined space
—		average value over wavelengths

Abbreviations

FID	flame ionization detector
LSRPA	local superficial rate of photon absorption
PTFE	polytetrafluoroethylene
RMSE	root mean square error
VOC	volatile organic compound

References

[1] D. A. Missia, E. Demetriou, N. Michael, E. I. Tolis, J. G. Bartzis, *Atmos. Environ.* **2010**, *44 (35)*, 4388–4395. DOI: 10.1016/j.atmosenv.2010.07.049

[2] S. Banerjee, S. C. Pillai, P. Falaras, K. E. O'Shea, J. A. Byrne, D. D. Dionysiou, *J. Phys. Chem. Lett.* **2014**, *5*, 2543–2554. DOI: 10.1021/jz501030x

[3] R. Daghrir, P. Drogui, D. Robert, *Ind. Eng. Chem. Res.* **2013**, *52*, 3581–3599. DOI: 10.1021/ie303468t

[4] Y. Ohko, D. A. Tryk, K. Hashimoto, A. Fujishima, *J. Phys. Chem. B* **1998**, *102*, 2699–2704. DOI: 10.1021/jp9732524

[5] A. Fujishima, T. N. Rao, D. A. Tryk, *J. Photochem. Photobiol., C* **2000**, *1*, 1–21. DOI: 10.1016/S1389- 5567(00)00002-2

[6] I. SopyanI, M. Watanabe, S. Murasawa, K. Hashimoto, A. Fujishima, *J. Photochem. Photobiol., A* **1996**, *98*, 79–86. DOI: 10.1016/1010-6030(96)04328-6

[7] E. Obuchi, T. Sakamoto, K. Nakano, *Chem. Eng. Sci.* **1999**, *54*, 1525–1530. DOI: 10.1016/S0009-2509(99)00067-6

[8] M. L. Sauer, D. F. Ollis, *J. Catal.* **1996**, *158*, 570–582. DOI: 10.1006/jcat.1996.0055

[9] M. Sung, S. Kato, F. Kawanami, M. Sudo, *Build. Environ.* **2010**, *45*, 2002–2007. DOI: 10.1016/j.buildenv.2010.03.007

[10] R. Asahi, T. Morikawa, T. Ohwaki, K. Aoki, Y. Taga, *Science* **2001**, *293*, 269–271. DOI: 10.1126/science.1061051

[11] S. Sakthivel, H. Kisch, *Angew. Chem. Int. Ed.* **2003**, *42*, 4908–4911. DOI: 10.1002/anie.200351577

[12] S. Sakthivel, H. Kisch, *ChemPhysChem* **2003**, *4*, 487–490. DOI: 10.1002/cphc.200200554

[13] K. Iketani, R.-D. Sun, M. Toki, K. Hirota, O. Yamaguchi, *Mater. Sci. Eng., B* **2004**, *108*, 187–193. DOI: 10.1016/j.mseb.2003.09.013

[14] K. Nishijima, B. Ohtani, X. Yan, T. Kamai, T. Chiyoya, T. Tsubota, N. Murakami, T. Ohno, *Chem. Phys.* **2007**, *339*, 64–72. DOI: 10.1016/j.chemphys.2007.06.014

[15] V. C. Papadimitriou, V. G. Stefanopoulos, M. N. Romanias, P. Papagiannakopoulos, K. Sambani, V. Tudose, G. Kiriakidis, *Thin Solid Films* **2001**, *520*, 1195–1201. DOI: 10.1016/j.tsf.2011.07.073

[16] E. Pulido Melián, O. González Díaz, A. Ortega Méndez, C. R. López, M. Nereida Suáez, J. M. Doña Rodríguez, J. A. Navío, D. Fernández Hevia, J. Pérez Peña, *Int. J. Hydrogen Energy* **2013**, *38*, 2144–2155. DOI: 10.1016/j.ijhydene.2012.12.005

[17] S. M. Zacarías, M. L. Satuf, M. C. Vaccari, O. M. Alfano, *Ind. Eng. Chem. Res.* **2012**, *51*, 13599–13608. DOI: 10.1021/ie3009956

[18] C. H. Liang, C. Y. Mou, D. J. Lee, *Chem. Eng. Sci.* **2005**, *60*, 1939–1952. DOI: 10.1016/j.ces.2004.11.038

[19] J. Yang, D. Li, Z. Zhang, Q. Li, H. Wang, *J. Photochem. Photobiol., A* **2000**, *137*, 197–202. DOI: 10.1016/S1010-6030(00)00340-3

[20] M. F. J. Dijkstra, H. J. Panneman, J. G. M. Winkelman, J. J. Kelly, A. A. C. M. Beenackers, *Chem. Eng. Sci.* **2002**, *57*, 4895–4907. DOI: 10.1016/S0009-2509(02)00290-7

[21] G. E. Imoberdorf, H. A. Irazoqui, A. E. Cassano, O. M. Alfano, *Ind. Eng. Chem. Res.* **2005**, *44*, 6075–6085. DOI: 10.1021/ie049185z

[22] A. E. Cassano, C. A. Martin, R. J. Brandi, O. M. Alfano, *Ind. Eng. Chem. Res.* **1995**, *34*, 2155–2201. DOI: 10.1021/ie00046a001

[23] D. K. Edwards, *Sol. Energy* **1977**, *19*, 401–402. DOI: 10.1021/ie00046a001

[24] R. Siegel, J. Howell, *Thermal Radiation Heat Transfer*, 4th ed., Taylor and Francis, New York **2002**.

[25] S. Walter, S. Malmberg, B. Schmidt, M. A. Liauw, *Catal. Today* **2005**, *110 (1–2)*, 15–25. DOI: 10.1016/j.cattod.2005.09.019

[26] R. K. Shah, A. L. London, *J. Heat Transfer* **1974**, *96 (2)*, 159–165. DOI: 10.1115/1.3450158

